# Large-scale and multiband silicon photonics wavelength cross-connect switch with FSR-free grating-assisted contra-directional couplers

Kazuhiro Ikeda, *Member, IEEE*, Ryotaro Konoike, *Member, IEEE*, and Keijiro Suzuki

*(Top-Scored Paper)*

*Abstract*— The recent advancement of cloud computing including AI applications requires a large networking capacity in datacenters resulting in a large power consumption at the same time. Optical switches significantly improve energy efficiency in datacenter networks, and silicon photonics enables the optical switch to operate faster than microseconds and be highly integrable for co-integration with GPUs. To support such high-capacity interconnect and switching, flexible use of multiple lanes and wavelength division multiplexing is essential, which can be implemented by a wavelength selective switch or wavelength cross-connect (WXC) switch. We proposed a novel silicon photonics WXC switch with free-spectral-range (FSR)-free grating-assisted contra-directional couplers (C-DCs) and Mach-Zehnder interferometers (MZIs), where extremely broadband operation is expected because of the unlimited FSR. In this paper, we demonstrate a largest ever port- and channel-count, 16 × 16 ports and 16 wavelength channels over the C+L-band, monolithically integrated WXC switch with 256 FSR-free grating-assisted C-DCs and 1,024 thermo-optic MZIs. Further extended multiband operation from the O-band to U-band will be potentially available by implementing two additional design considerations.

*Index Terms*— Integrated photonics, Optical switch, Silicon photonics, Wavelength cross-connect

## I. INTRODUCTION

THE advancement of switch ICs for datacenter networks is prominent and the bandwidth is expected to reach 100 Tbps in 2024 [1]. However, the power consumption is also increasing at the same time as 300, 450, and 500 W for the recent switch ICs with bandwidths of 12.8, 25.6 and 51.2 Tbps, respectively [2][3]. The 100-Tbps switch IC should consume more power. Optical switches, on the other hand, significantly improve switching energy efficiency. We previously demonstrated a much lower power consumption of 18 and 24 W for 35.2 [4] and 81.9 Tbps [5], respectively, for our fully packaged silicon photonics switches [6]. Recently, Google announced that they started using optical circuit switching (OCS) in their datacenters, where only spine switches were replaced by optical switches based on free-space optics with a MEMS mirror array, resulting in 30% less cost and 41% less power [7]. In addition, Google also announced that TPU v4, their supercomputer for Machine Learning, also utilizes the OCS [8]. Currently, their optical switch is used for topology engineering with low frequency updates, and the main traffic engineering is still done with electrical switches. If optical switches are to be introduced to a wider range in datacenters, a switching time of microseconds or less will be required instead of the millisecond switching time in the MEMS optical switch. Also, generative AI models such as ChatGPT are currently a very hot topic. To configure such a large AI model with a huge number of parameters reaching to 1,000 billion, a lot of GPUs are connected by ultrahigh bandwidth interconnects and switches. For example, nVIDIA offers a system networking the maximum 256 GPUs with 57.6TB/s in all-to-all connection [9]. For higher bandwidth density and lower energy per bit, use of optical switching has been proposed [10][11], where a very large-scale silicon photonics circuit and switch is to be co-integrated with multiple GPUs. For the above-mentioned applications of datacenter networks and GPU clusters, optical switches based on silicon photonics offer fast switching in the order of microseconds or less and high integrability for co-integration with GPUs.

To support such a large interconnect capacity exceeding 100 Tbps, use of multiple lanes and wavelength division multiplexing (WDM) is essential. Therefore, we need to introduce wavelength selectivity to the silicon photonics switch, in other words, to develop a wavelength selective switch or wavelength cross-connect (WXC) switch for flexible networking of wavelength channels. For example, each wavelength channel from a node connects to each node in one case, a bundle of multiple wavelength channels connects to a specific node with a higher link capacity in another case, and so on. There have been different approaches for the WXC switch, such as Echelle gratings with waveguide MEMS [12], thermo-

Color versions of one or more of the figures in this article are available online at https://ieeexplore.ieee.org.

optic (TO) ring resonators in crossbar arrangement [13], and TO ring resonators with Mach-Zehnder interferometers (MZIs) [14]. However, since these devices are based on high order diffraction or resonance, the free spectral range (FSR) fundamentally limits the available bandwidth. There are approaches to improve the limitation, but it will make the devices complicated and the improvement will be limited. We previously proposed a novel approach to use FSR-free grating-assisted contra-directional couplers (C-DCs) and MZIs, where extremely broadband operation is expected because of the unlimited FSR [15][16]. The silicon photonics C-DCs consist of two coupled waveguides with sidewall corrugation that induces mode coupling between the waveguides in the counter direction at a Bragg wavelength [17]. Due to the first order operation, the C-DC has practically an unlimited FSR and is suitable for multiband add-drop filters. In addition, the large index modulation of the silicon waveguide corrugation induces a large coupling coefficient leading to a wide and flattop spectral shape, which offers high tolerance for temperature change and is suited for cost effective coarse WDM systems. Very recently, we extended our proposed WXC architecture to the largest ever scale of 16 × 16 ports and 16 wavelength channels [18] (the previous largest one for monolithically integrated WXC was 8 × 8 ports and 8 wavelength channels [12]), where 256 FSR-free grating-assisted C-DCs and 1,024 TO-MZIs were integrated on a 11 mm × 26 mm silicon chip. In this paper, we comprehensively explain our proposed WXC switch and provide extended details on the 16 × 16 16-ch WXC switch including discussions on impact of waveguide intersections and design considerations for further extended multiband operation.
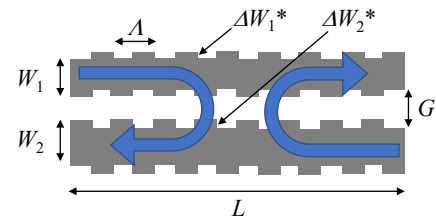
## II. Grating-Assisted Contra-Directional Coupler

Figure 1 describes the C-DC consisting of two coupled silicon waveguides with the waveguide widths, $W_1$ and $W_2$, the sidewall grating depths, $\Delta W_1$ and $\Delta W_2$, the sidewall grating period, $\Lambda$, the gap between the waveguides, $G$, and the length of the C-DC, $L$. In this structure, there is the Bragg condition for contra-directional cross coupling between the guided modes as described by the blue arrows [17],

$$\beta_1 + \beta_2 = \frac{2\pi}{\Lambda}, \quad (1)$$

where $\beta_1$ and $\beta_2$ are the propagation constants of the modes in the waveguide 1 and 2, respectively. Thus, $\Lambda$ for a target channel wavelength $\lambda$ can be determined by,

$$\Lambda = \frac{\lambda}{n_1(\lambda) + n_2(\lambda)}, \quad (2)$$

where $n_1$ and $n_2$ are the effective index of the propagation modes in the waveguide 1 and 2, respectively. We can also determine $\Delta W_1$, $\Delta W_2$, $G$ $(L)$ to design the bandwidth (extinction) of the cross coupling. The reflection in the same waveguide, whose Bragg condition is given by $\beta_{1,2} = \pi/\Lambda$, can be removed by $\pi$ phase shift between gratings on each side of waveguide



Fig. 1. Schematic diagram of C-DC: Two coupled silicon waveguides with the waveguide widths, $W_1$ and $W_2$, the sidewall grating depths, $\Delta W_1$ and $\Delta W_2$, the sidewall grating period, $\Lambda$, the gap, $G$, and the length, $L$. The blue arrows show the contra-directional cross coupling between the guided modes at the Bragg condition.



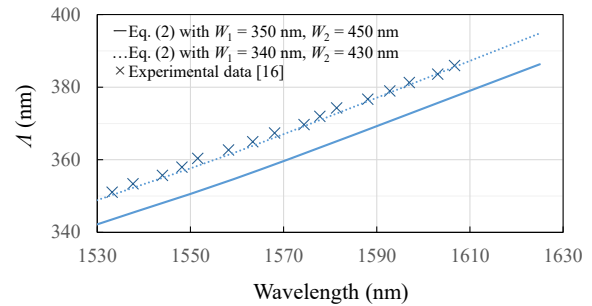Fig. 2. Calculated $\Lambda$ from Eq. (2) and experimental data from [16] ($W_1 = 350$ nm and $W_2 = 450$ nm, and waveguide height is 220 nm). Dotted line shows calculated $\Lambda$ with $W_1 = 340$ nm and $W_2 = 430$ nm.

[19]. We have no FSR (or more precisely, an extremely wide FSR) due to the 1-st order operation in this device. Figure 2 plots the calculated $\Lambda$ from Eq. (2) and the experimental data from [16], where $W_1 = 350$ nm and $W_2 = 450$ nm, and the waveguide height is 220 nm. The $W_1$ and $W_2$ are selected so that the waveguides have a single mode around the operation band as will be revisited in the section V. The waveguide height is based on a recent standard silicon-on-insulator wafer that has 220-nm top silicon thickness. The $n_1$ and $n_2$ are calculated by the finite element method. The calculated $\Lambda$ (solid line) is slightly off from the experimental data (cross marks) probably because the fabricated waveguide widths were slightly narrower than the design value and the corrugated waveguides had a slightly lower effective index than the straight waveguide. If we use $W_1 = 340$ nm and $W_2 = 430$ nm instead, the calculated $\Lambda$ fit well to the experimental data as shown by the dotted line.

## III. Wavelength Cross-Connect Switch Architecture

Figure 3 explains the $N \times N$ and $N_\lambda$-channel WXC switch architecture using the C-DCs and MZI-based switches [15], where two sets of 4-channel WDM signals are introduced into the input ports labeled as 1 and 2 and guided respectively to 4 different output ports. The channel described by the solid blue arrow is dropped by the first C-DC designed for $\lambda_1$ and switched to the second output port from the top in the switch also designed for $\lambda_1$, then guided to the upper waveguide through another C-DC. The channel described by the solid red arrow is dropped by the second C-DC designed for $\lambda_2$ and switched to the top output port in the switch also designed for $\lambda_2$, then
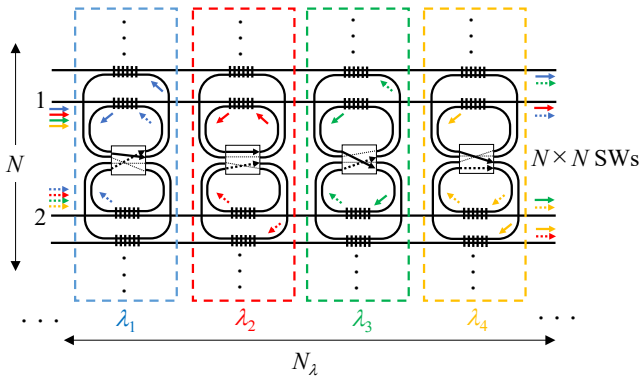
Fig. 3. $N \times N$ and $N_\lambda$-channel WXC switch architecture with the C-DCs and MZI-based switches. Two sets of 4-channel WDM signals (solid and dotted arrows) are introduced into the input ports labeled as 1 and 2 and guided to 4 different output ports.

TABLE I
STRUCTURE DIMENSIONS OF C-DCS FOR 16 × 16 16-CH WXC SWITCH

| Symbol | Dimension | Nominal Value |
|---|---|---|
| $W_1, W_2$ | Waveguide widths | 350 nm, 450 nm |
| $G$ | Gap between waveguides | 250 nm |
| $L$ | Length of C-DC | ~800 μm |
| $\Lambda$ | Period of grating | $352 \sim 388$ nm |
| $\Delta W_1, \Delta W_2$ | Depth of grating | $30 \sim 40$, $50 \sim 60$ nm |
| - | Apodization | Gaussian |

dimensions, and apodization, the Bragg length (or the reciprocal of contra-directional coupling coefficient) was numerically calculated to be larger than 200 μm [16]. For sufficient extinction, we selected $L$ longer enough than the Bragg length. The layout of a 16 × 16 switch and 16 C-DCs designed for a single wavelength channel is depicted in Fig. 4(a).

guided to the same waveguide trough the same C-DC. In the same way, the other 2 channels described by the solid green and yellow arrows are switched and guided to the lower 2 waveguides. The other set of WDM signal described by the dotted arrows are also guided differently at the same time as described in the same figure. We can introduce the other WDM signals into the other input ports at the same time. The port count can be increased by adding C-DCs and waveguides in the upper and lower direction, and by increasing the port count of the switches. The number of wavelength channel can be increased by cascading C-DCs and switches in the left and right direction.

The waveguide intersection in a WXC switch circuit is an important component to determine the loss and crosstalk of the device. The maximum number of waveguide intersections scales with $2 \times (N-1) \times (N_\lambda - 1)$ in a conventional WXC switch architecture [12] while with $2 \times (N2 - 1) \times N_\lambda$ in our architecture, which is about a half of the conventional one and is another advantage of our WXC switch architecture. However, if we consider the broadband or multiband operation in our WXC switch architecture shown in Fig.3, the available bandwidth of the waveguide intersections will be a limiting factor. The waveguide intersections should cover the full operation bandwidth designated for the WXC switch, while the CD-Cs and $N \times N$ switches are designed for each channel wavelength and it is enough for them to cover a narrow band. The details will be discussed in the section IV.C.

## IV. C + L-BAND 16 × 16 16-CHANNEL SILICON PHOTONICS WAVELENGTH CROSS-CONNECT SWITCH

### A. Design and Fabrication

Table 1 summarizes structure dimensions of C-DCs for the 16 × 16 16-ch WXC switch. We used $W_1 = 350$ nm, $W_2 = 450$ nm, $G = 250$ nm, $L \sim 800$ μm, $\Lambda = 352 \sim 388$ nm, $\Delta W_1 = 30 \sim 40$ nm, and $\Delta W_2 = 50 \sim 60$ nm. $\Delta W_1$ and $\Delta W_2$ were varied for each wavelength channel to equalize the bandwidth of the cross-coupling and they were also Gaussian-apodized (Other apodization window functions may be applied). The value of $G$ was determined based on the gap of our standard directional coupler design, which provides reliable fabrication and decent mode field overlap. With the above $G$, waveguide/grating
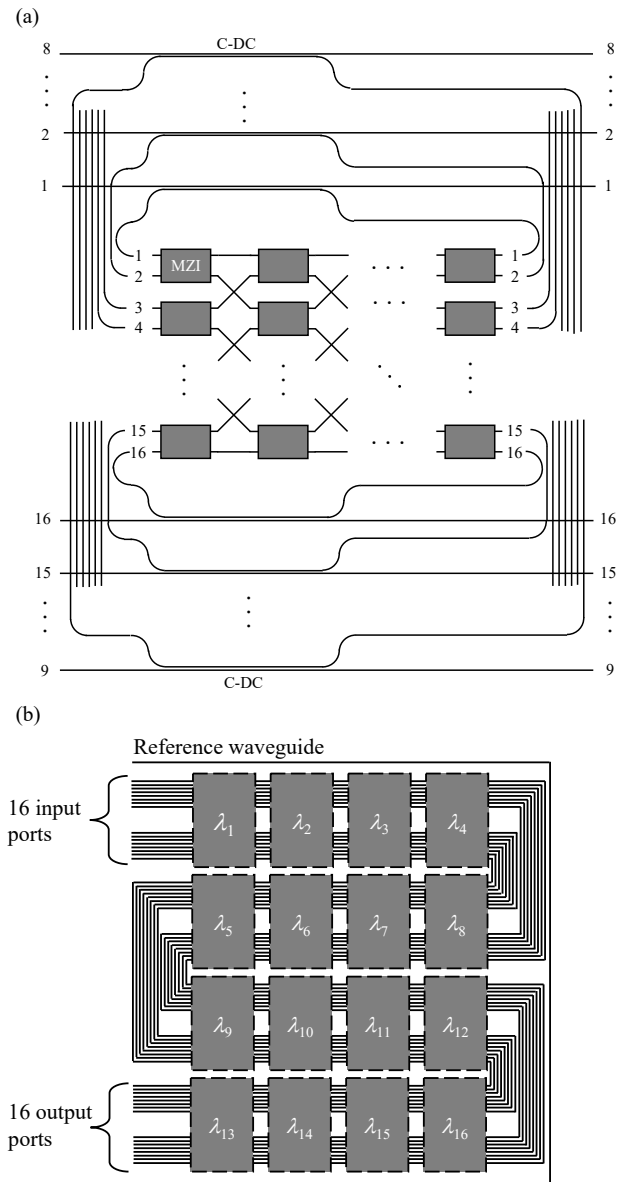


Fig. 4. (a) Layout of a 16 × 16 switch and 16 C-DCs designed for a single wavelength channel. The 16 × 16 switch consists of 64 MZIs (an 8 × 8 array of 2 × 2 TO switches) and waveguide intersections in between. (b) Circuit layout of the 16 × 16 16-ch WXC switch. Wavelength switch circuits surrounded by the dotted lines correspond to the circuit in (a).

The 16 × 16 switch consists of 64 MZIs (an 8 × 8 array of 2 × 2 TO switches) and waveguide intersections in between. We used the optimized designs of the building blocks such as MZIs and waveguide intersections that we have developed in the past works of large-scale silicon photonics switches [6]. Note that this usage of the 8 × 8 matrix of MZIs as a 16 × 16 switch results in a blocking switch. In another usage, we can obtain two synchronous sets of 8 × 8 strictly non-blocking switch (path-independent insertion loss (PILOSS) switch) with a unique port assignment [20]. We drew the 16 × 16 16-ch silicon photonics WXC circuit as shown in Fig. 4(b) so that the overall circuit is densely packed. The wavelength switch circuits surrounded by the dotted lines correspond to the circuit shown in Fig. 4(a). All the input and output ports were placed on one side of the chip with a pitch of 250 μm. A reference waveguide surrounding the whole circuit was also included for fiber array alignment and estimation of the fiber-to-chip coupling loss. TE-pass polarizers were integrated into all the input and output ports to suppress the TM light since the WXC is designed for the TE mode.

We fabricated the 16 × 16 16-ch silicon photonics WXC chip using our 300-mm CMOS pilot line with 45-nm ArF immersion
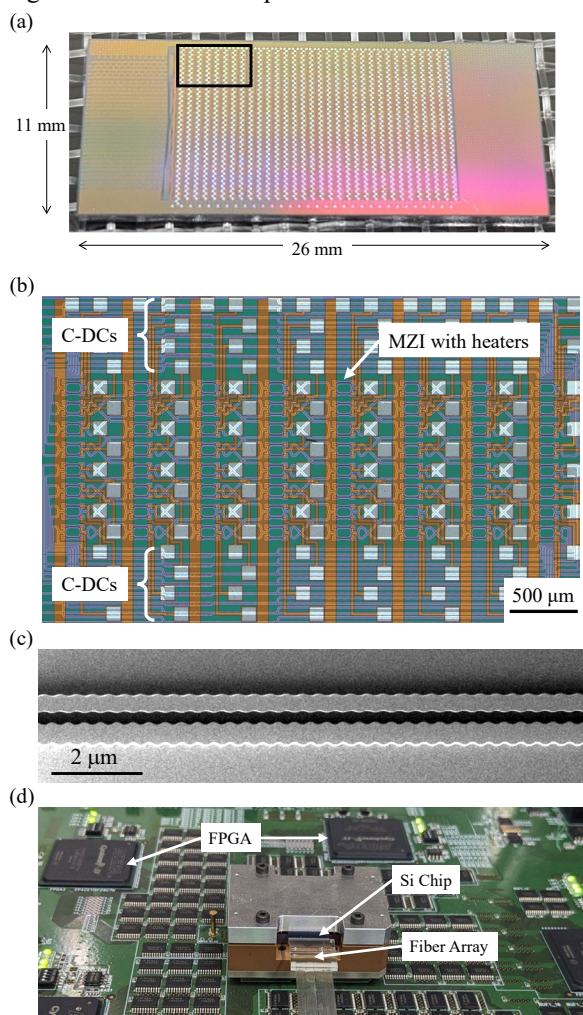


Fig. 5. (a) Photograph of the fabricated 16 × 16 16-ch silicon photonics WXC chip where 256 C-DCs, 1,024 MZIs and 2,048 microheaters were integrated. (b) Micrograph of a 16 × 16 switch and 16 C-DCs for a single wavelength channel (area surrounded by the black square in (a)). (c) SEM image of a C-DC taken before silicon dioxide cladding deposition. (d) Assembled device inserted into the socket on the control circuit board with FPGAs.

lithography [6]. Figure 5(a) shows a photograph of the fabricated 11 mm × 26 mm chip where 256 C-DCs (16 ports × 16 wavelengths), 1,024 MZIs (64 MZIs × 16 wavelengths) and 2,048 microheaters (64 MZIs × 2 × 16 wavelengths) were integrated. A magnified view of a 16 × 16 switch and 16 C-DCs for a single wavelength channel surrounded by the black square in Fig. 5(a) is shown in Fig. 5(b). Note that a waveguide intersection was placed after each MZI to exchange the bar and the cross ports. This can improve the leakage at the bar port of the 2 × 2 switch which is useful when operated as two synchronous PILOSS switches [6]. An SEM image of a C-DC taken before silicon dioxide cladding deposition is also shown in Fig. 5(c). The WXC chip with more than 2,000 electrical pads was first flip-chip bonded to a ceramic interposer to extend the pad arrangement to a 0.5-mm land grid array, then attached by a 34-port high-NA fiber array with an MFD of ~ 4 μm. The assembled device was inserted into the socket on the control circuit board as shown in Fig. 5(d). 5 FPGAs on the control circuit board were clocked by a 50-MHz quarts oscillator and synchronized with 1-MHz timing each other. Each FPGA connected by buffer ICs generated a rectangular pulse sequence (5 V amplitude, 1 MHz repetition), whose duty cycle was tuned to adjust applied power to the heater. With pre-emphasis control we previously demonstrated using the same circuit board [6], the switching time of the WXC switch is expected to be less than 3 μs.

### B. Characterization

TE-polarized C + L band ASE light was introduced to the input port 8 of the WXC (See Fig. 4(a) for the port number allocation). We routed one of the 16 wavelength channels to the output port 9 (8-to-9 connection, drop) while the other channels to the output port 8 (8-to-8 connection, through) and measured the transmission spectra from the output port 8 and 9 using an optical spectrum analyzer. We repeated this for the 16 wavelength channels and the results are shown in Fig. 6(a) and (b) respectively. Also shown in Fig. 6(c) is transmission spectra from the output port 8 (red) and 9 (blue) for another example
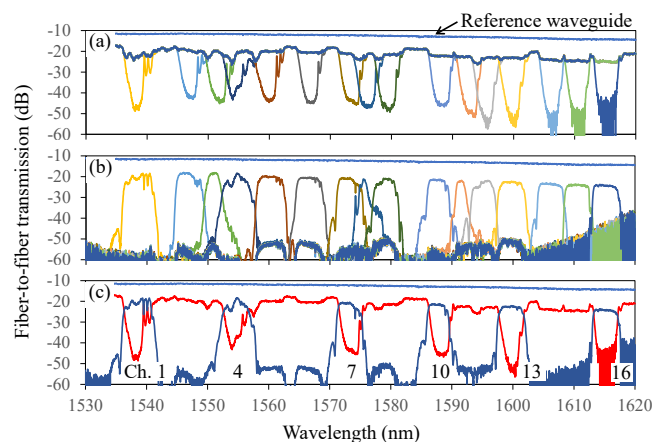


Fig. 6. Transmission spectra from (a) output port 8 and (b) output port 9, when TE-polarized C + L band ASE light was introduced to the input port 8 of the 16 × 16 16-ch WXC switch, and each of the 16 wavelength channels was set to the 8-to-9 connection while the other channels were set to the 8-to-8 connection. (c) Transmission spectra from output port 8 (red) and 9 (blue) when channels 1, 4, 7, 10, 13, and 16 were, at the same time, set to the 8-to-9 connection while the other channels were set to the 8-to-8 connection.

switching state, where channels 1, 4, 7, 10, 13, and 16 were, at the same time, set to the 8-to-9 connection while the other channels were set to the 8-to-8 connection. We can see that the 16 channels are distributed over a wide wavelength range of the C and L bands. The bandwidth of the wavelength channels is around 4 nm. The channels 3, 8, and 11 are overlapped with the adjacent channels and have narrower bandwidths in Fig. 6(b). This is because the overlapped spectral component routed to port 9 is again routed to some other port by the adjacent C-DC and switch. The transmission spectrum of the reference waveguide was also measured and plotted in the Figs. 6(a)-(c). The fiber-to-fiber transmission of the reference waveguide is −11.5 dB at 1550 nm, from which the fiber-to-chip coupling loss is estimated as 3.1 dB/facet by subtracting the loss of the
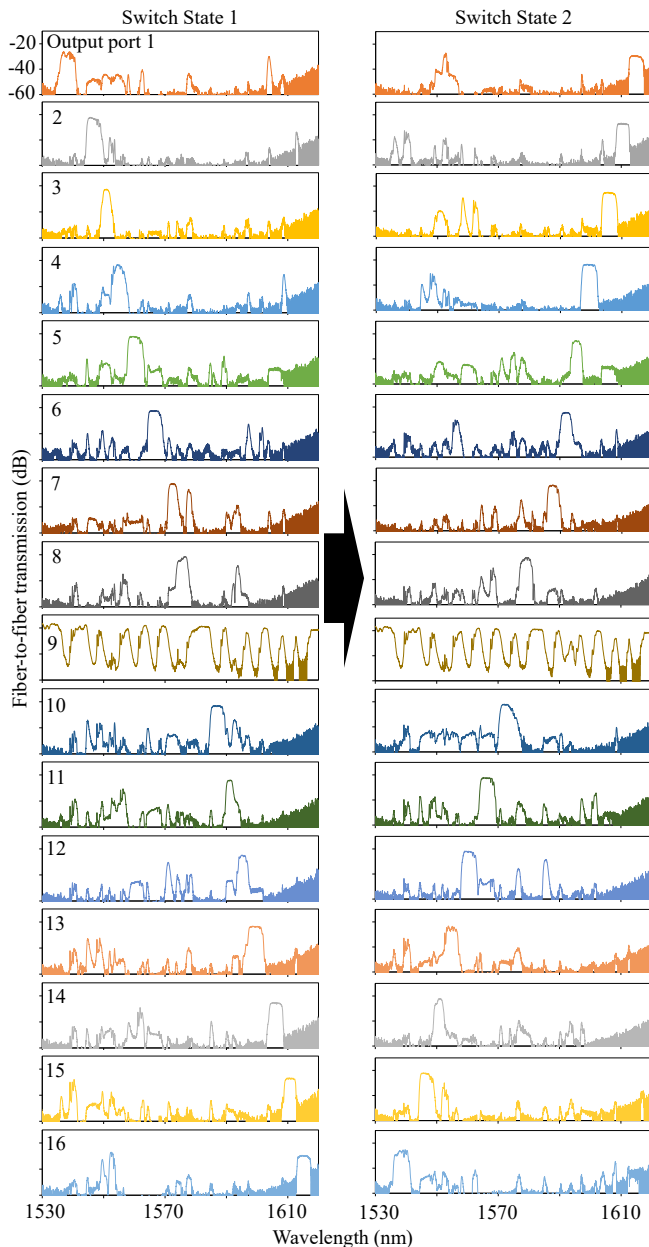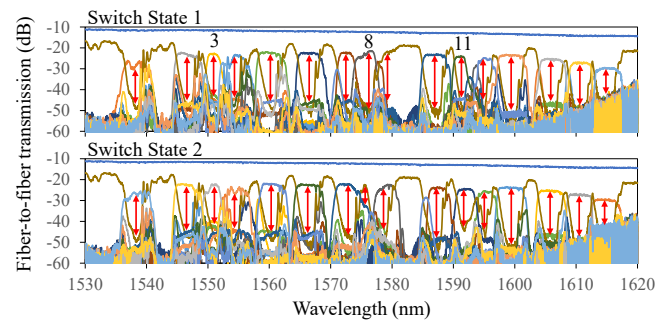


Fig. 8. Overlayed plots of all the 16 spectra for two switch states (Replots of Fig.7).

waveguide. In Fig. 6(a), a transmission difference between the reference waveguide and the 8-to-8 connection at around 1585 nm (this wavelength was outside of any C-DC band and passed through the 16 C-DCs) is read as ~6 dB. Considering a transmission difference of 3.2 dB from the waveguide length difference, we estimate a loss of the single C-DC to be ~0.18 dB by $(6 - 3.2) / 16$. A loss increase at a C-DC center wavelength of 1588 nm from the loss at ~1585 nm is ~3.5 dB, which corresponds to a loss of the $16 \times 16$ MZI-based switch. An on-chip loss of the WXC is then estimated to be $11.5 + 6 + 3.5 - 3.1 \times 2 = 14.8$ dB.

Next, the ASE light was introduced to the input port 9. The wavelength channels 1, 2, 3…, were routed to the output port 1, 2, 3…, and then switched to the output port 16, 15, 14…, respectively. The measured spectra from all the 16 output ports at the two switch states are shown in Fig. 7. We can see successful switching while some peaks outside each channel band. These spectral peaks originate from the spectral overlaps between adjacent channels explained above (especially, the channels 3, 8, and 11 and their adjacent channels), and therefore are off the channel center wavelengths. The overlapped spectral component is dropped and switched twice by the adjacent C-DCs and switches and therefore routed to a non-target port. In order to clarify this point, all the 16 spectra were overlayed for the two switch states in Fig. 8. We can see that the on-off spectral windows marked by red arrows of the channels 3, 8, and 11 and their adjacent channels are significantly affected by the overlapped spectral components and become narrower. These spectral overlaps will be minimized by appropriate wavelength and bandwidth allocation.

### C. Impact of Waveguide Intersection

In Fig. 8, we observe the transmission difference between the wavelength channels. For example, the transmissions of channel 1 (~1538 nm) and 16 (~1615 nm) are ~4 dB and ~6 dB lower than the channel 8 (~1576 nm). This transmission difference originates from the number of passing waveguide intersections and the wavelength dependence of the transmission of the waveguide intersection. Here, we consider the details for the channel 1, 8 and 16 in the switch state 1 using Fig. 4 (a) and (b). The light of the channel 1 is dropped from the waveguide connected to the input port 9 (waveguide 9) and routed to the waveguide connected to the output port 1 (waveguide 1) by the first wavelength switch $\lambda_1$. From Fig. 4(a), the number of passing waveguide intersections in the wavelength switch $\lambda_1$ can be counted as 7 (before the $16 \times 16$



Fig. 7. Transmission spectra from all the 16 output ports at the two switch states where the wavelength channels 1, 2, 3…, were routed from the input port 9 to the output port 1, 2, 3…, and then to the output port 16, 15, 14…, respectively.

switch) + 16 (inside the 16 × 16 switch including 8 for each MZI's outport exchange) + 7 (after the C-DC on waveguide 1) = 30. After the wavelength switch $\lambda_1$, the light of the channel 1 passes 14 waveguide intersections on the waveguide 1 in each wavelength switch $\lambda_2 \sim \lambda_{16}$, resulting in 14 × 15 = 210. The total number of passing waveguide intersection for the channel 1 is therefore 240. Note that this is the maximum case for our WXC architecture, i.e. $2 \times (N/2 - 1) \times N_\lambda = 224$ with $N = N_\lambda = 16$, plus 16 waveguide intersections inside the 16 × 16 switch. Since the waveguide intersection was optimized for ~1550 nm [6] and the loss at ~1538 nm was measured as 0.02 dB in a test sample, the loss for the channel 1 originating from the passing waveguide intersections will be 240 × 0.02 = 4.8 dB. The channel 8 passes only 30 waveguide intersections in the wavelength switch $\lambda_8$ because the waveguides 9 and 8 (before and after the wavelength switch $\lambda_8$) have no waveguide intersection. Since the loss of the waveguide intersection at ~1576 nm was measured as 0.05 dB in a test sample, the loss for the channel 8 originating from the passing waveguide intersections will be 30 × 0.05 = 1.5 dB. The loss difference between the channel 1 and 8 estimated above (3.3 dB) is consistent with the observed value of ~4 dB. Similarly, the channel 16 passes 30 waveguide intersections in the wavelength switch $\lambda_{16}$ and 14 waveguide intersections on the waveguide 16 in each wavelength switch $\lambda_{13} \sim \lambda_{15}$ (no waveguide intersection on the waveguide 9 before the wavelength switch $\lambda_{16}$) resulting in 30 + 14 × 3 = 72. Since the loss of the waveguide intersection at ~1615 nm was measured as 0.09 dB in a test sample, the loss for the channel 16 originating from the passing waveguide intersection will be 72 × 0.09 = 6.5 dB. The estimated loss difference between the channel 1 and 16 (5 dB) is close to the observed value of ~6 dB.

As discussed above, a very low loss over a broad wavelength band of the waveguide intersection is of critical importance for the broadband and large-port-count WXC switch.

## V. DESIGN CONSIDERATIONS FOR EXTENDED MULTIBAND OPERATION

Since our WXC switch uses the FSR-free C-DCs, further extended multiband operation from the O-band to U-band will be potentially available. To achieve such operation, two design considerations should be implemented. The first design consideration is for the ultrabroad band waveguide intersection. As discussed in IV. C., the wa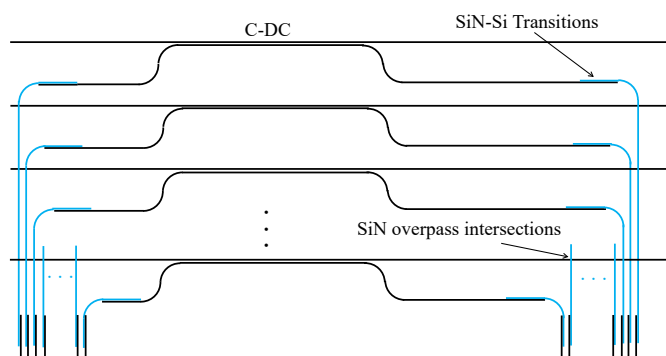veguide intersection used in this work has an adequately low loss around the designed wavelength (0.02 dB at around 1550 nm), but an increased loss at a wavelength apart from the designed wavelength (0.09 dB at around 1570 nm). While this type of waveguide intersection can be used inside the $N \times N$ switches because it can be optimized for each channel wavelength [21], an ultrabroad band design is necessary for the waveguide intersections on the waveguides connected to the input and output ports where any wavelength channel passes. One possible option will be the silicon nitride waveguide overpass intersection [22], which has a negligibly small crossing loss for any wavelength. The usage of the silicon nitride overpass intersections in our WXC switch is described in Fig. 9. The transition from a silicon waveguide to a silicon nitride waveguide based on directional coupling can be optimized for each channel wavelength (not necessary to cover all the wavelengths).

The second design consideration is for higher order modes in the C-DC. In this work, the C-DC was designed with $W_1 = 350$ nm, $W_2 = 450$ nm, and a waveguide height of 220 nm, and the two waveguides (waveguide 1 and 2, respectively) had only a single mode (TE0) in the C- and L-band. Therefore, a single Bragg condition between the two fundamental modes (TE0-TE0) was considered. However, the waveguide 2 has a higher order mode (TE1) in the O-band, which causes an additional Bragg condition between the TE0 mode in the waveguide 1 and the TE1 mode in the waveguide 2 (TE0-TE1). Figure 10 plots the calculated $\Lambda$ from Eq. (2) for the two cases over the extended wavelength region from the O-band to the U-band. By changing $\Lambda$ from 240 to 410 nm, the Bragg wavelength for TE0-TE0 can be allocated over the O-band to the U-band. However, the C-DCs with $\Lambda$ of from 300 to 350 nm cause not only the TE0-TE0 cross couplings for the channel wavelengths of from 1430 to 1550 nm but also the TE0-TE1 cross couplings for the channel wavelengths of from 1260 to 1360 nm. Therefore, the current design with $W_1 = 350$ nm, $W_2 = 450$ nm does not work for the full O to U band but may work for the E to U band or the O + L + U band excluded 1430 to 1550 nm. The WXC switch operating in the full O to U band can be designed by using a waveguide pair with narrower waveguide widths cutting off the higher order mode.
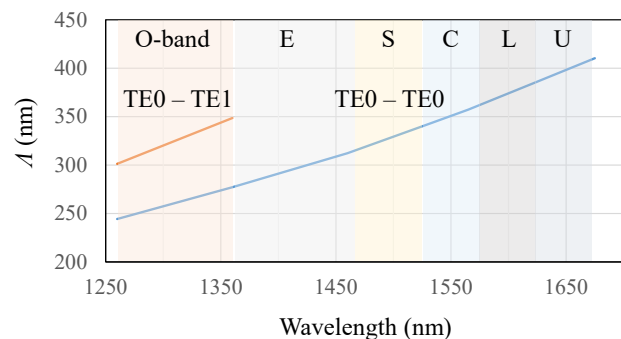


Fig. 10. Calculated $\Lambda$ from Eq. (2) for Bragg conditions between two fundamental modes (TE0-TE0) and between the TE0 mode and the TE1 mode (TE0-TE1) in the waveguide 1 and 2 of C-DC over the extended wavelength region from the O-band to the U-band ($W_1 = 350$ nm and $W_2 = 450$ nm, and waveguide height is 220 nm).



Fig. 9. Schematic of usage of silicon nitride overpass intersections for extended multiband operation.

## VI. CONCLUSIONS

We have demonstrated a C+L-Band 16 × 16 16-ch silicon photonics WXC based on C-DCs and MZIs. Since the operation bandwidth of this WXC is not limited by FSR, a design for further extended multiband operation over from the O-band to the U-band is possible, which will be useful for future multiband network systems.

## REFERENCES

[1] https://blogs.cisco.com/sp/co-packaged-optics-and-an-open-ecosystem

[2] https://www.broadcom.com/products/ethernet-connectivity/switching/strataxgs/bcm56990-series

[3] https://www.theregister.com/2022/08/16/broadcom_nvidia_switch/

[4] T. Kurosu, T. Inoue, K. Suzuki, S. Suda, and S. Namiki, "Fully-Loaded and Cascaded Operation of Polarization-Diversity 8 × 8 Silicon Photonics Optical Switch with 11-ch × 32/44-Gbaud DP-16QAM WDM Transmission," Optical Fiber Communication Conference (OFC) 2018, PDP Th4D.3

[5] R. Matsumoto, R. Konoike, K. Suzuki, H. Matsuura, K. Ikeda, T. Inoue, and S. Namiki, "Fully-Loaded Operation of 0.29-pJ/bit Wall-plug Efficiency, 81.9-Tb/s Throughput 32 × 32 Silicon Photonics Switch," Optical Fiber Communication Conference (OFC) 2021, Tu6A.2

[6] K. Ikeda, K. Suzuki, R. Konoike, S. Namiki, and H. Kawashima, "Large-scale silicon photonics switch based on 45-nm CMOS technology," Opt. Commun. 466, p. 125677 (2020).

[7] L. Poutievski, O. Mashayekhi, J. Ong, A. Singh, M. Tariq, R. Wang, J. Zhang, V. Beauregard, P. Conner, S. Gribble, R. Kapoor, S. Kratzer, N. Li, H. Liu, K. Nagaraj, J. Ornstein, S. Sawhney, R. Urata, L. Vicisano, K. Yasumura, S. Zhang, J. Zhou, and A. Vahdat, "Jupiter evolving: transforming google's datacenter network via optical circuit switches and software-defined networking," Proceedings of the ACM SIGCOMM 2022 Conference, New York, NY, USA, 66–85.

[8] N. Jouppi, G. Kurian, S. Li, P. Ma, R. Nagarajan, L. Nai, N. Patil, S. Subramanian, A. Swing, B. Towles, C. Young, X. Zhou, Z. Zhou, and D. A. Patterson, "TPU v4: An Optically Reconfigurable Supercomputer for Machine Learning with Hardware Support for Embeddings," Proceedings of the 50th Annual International Symposium on Computer Architecture (ISCA '23), New York, NY, USA, Article 82, 1–14.

[9] https://www.nvidia.com/en-us/data-center/nvlink/

[10] N. Harris, "Passage: A Wafer-Scale, Programmable Photonic Communication Substrate," Hot Chips 34, Session 2, Aug 2022.

[11] S. Zhang, Z. Zhang, M. Naderan-Tahan, H. SeyyedAghaei, X. Wang, H Li, S. Qin, D. Colle, G. Torfs, M. Pickavet, J. Bauwelinck, G. Roelkens, and L. Eeckhout, "Photonic Network-on-Wafer for Multichiplet GPUs," IEEE Micro 43, pp. 86-95 (2023).

[12] T. J. Seok, J. Luo, Z. Huang, K. Kwon, J. Henriksson, J. Jacobs, L. Ochikubo, R. S. Muller, and M. C. Wu, "Silicon photonic wavelength cross-connect with integrated MEMS switching," APL Photonics 4, 100803 (2019).

[13] A. S. P. Khope, M. Saeidi, R. Yu, X. Wu, A. M. Netherton, Y. Liu, Z. Zhang, Y. Xia, G. Fleeman, A. Spott, S. Pinna, C. Schow, R. Helkey, L. Theogarajan, R. C. Alferness, A. A. M. Saleh, and J. E. Bowers, "Multi-wavelength selective crossbar switch," Opt. Express 27, pp. 5203–5216 (2019).

[14] G. Van Steenberge, G. Roelkens, P. Ossieur, J. Missinne, J. Van Asch, J. Zhang, S. Qin, J. Van Campenhout, J. Van Kerkhof, M. M. Milosevic, P. Bakopoulos, D. Syrivelis, E. Mentovich, K. Morozov, S. Stracca, A. Bigongiari, T. Joerg, D. Schlick, T. Braun, M. W¨ohrmann, R. Gernhardt, Q. Cheng, T. Li, and R. Penty, "Packaging of Ultra-dynamic Photonic Switches and Transceivers for Integration into 5G Radio Access Network and Datacenter Sub-systems," IEEE 73rd Electronic Components and Technology Conference (ECTC 2023), p. 742. Orlando, FL, May 2023.

[15] K. Ikeda, K. Suzuki, R. Konoike, and H. Kawashima, "Silicon Photonics Wavelength Selective Switch with Unlimited Free Spectral Range," J. Lightwave Technol. 38, pp. 3268–3272 (2020).

[16] K. Ikeda, R. Konoike, K. Suzuki, H. Kawashima, "2 × 2 16-ch silicon photonics wavelength-selective switch based on waveguide gratings," Opt. Express 28, pp. 26861-26869 (2020).

[17] K. Ikeda, M. Nezhad, and Y. Fainman, "Wavelength selective coupler with vertical gratings on silicon chip," Appl. Phys. Lett. 92, 201111 (2008).

[18] K. Ikeda, R. Konoike, K. Suzuki, "C+L-Band 16 × 16 16-Channel Silicon Photonics Wavelength Cross-Connect Switch Based on Waveguide Bragg Gratings," European Conference on Optical Communications (ECOC) 2023, Glasgow, Scotland, Oct 2023.

[19] W. Shi, H. Yun, C. Lin, M. Greenberg, X. Wang, Y. Wang, S. T. Fard, J. Flueckiger, N. A. F. Jaeger, and L. Chrostowski, "Ultra-compact, flat-top demultiplexer using anti-reflection contra-directional couplers for CWDM networks on silicon," Opt. Express 21(6), 6733–6738 (2013).

[20] K. Tanizawa, K. Suzuki, K. Ikeda, S. Namiki, and H. Kawashima, "Novel polarization diversity without switch duplication of a Si-wire PILOSS optical switch," Opt. Express 24, 6861-6868 (2016).

[21] K. Suzuki, R. Konoike, G. Cong, K. Yamada, S. Namiki, H. Kawashima, K. Ikeda, "Strictly Non-Blocking 8 x 8 Silicon Photonics Switch Operating in the O-Band," J. Lightwave Technol. 39, 1096-1101 (2021).

[22] R. Konoike, K. Suzuki, K. Tanizawa, S. Suda, H. Matsuura, S. Namiki, H. Kawashima, and K. Ikeda, "SiN/Si double-layer platform for ultralow-crosstalk multiport optical switches," Opt. Express 27, 21130-21141 (2019).

**Kazuhiro Ikeda** (M'14) received the B.E. and M.E. degrees in precision science from Osaka University, Suita, Japan, in 1998 and 2000, respectively, and the Ph.D. degree in electrical engineering (Photonics) from the University of California, San Diego (UCSD), La Jolla, USA, in 2008. His doctoral thesis was on nonlinear optical responses in silicon nitride and amorphous silicon and sidewall corrugated waveguide devices, all for silicon photonics applications.

From 2000 to 2004, he was with Furukawa Electric Co., Ltd. working on polarization controllers and polarization mode dispersion compensators for optical fiber communications. In 2009, he joined the Graduate School of Materials Science, Nara Institute of Science and Technology, Ikoma, Japan, as an Assistant Professor, where he studied opto-spintronics and plasmonic microresonators for semiconductor lasers. Since 2014, he has been with the National Institute of Advanced Industrial Science and Technology, Tsukuba, Japan. Dr. Ikeda is a Senior Member of Optica, a Member of the IEICE, JSAP, IEEE Photonics Society. He was the recipient of the World Cultural Council Special Recognition 2019 and the 69th Electrical Science and Technology Encouragement Award. His research interests include silicon photonic integrated circuits and hybrid nanophotonics on silicon.

**Ryotaro Konoike** received the M.Eng. and Ph.D. degrees from the Department of Electronic Science and Engineering, Kyoto University, Kyoto, Japan, in 2014 and 2017, respectively. At Kyoto University, he studied integrated manipulation of photons on a photonic crystal chip containing multiple coupled nanocavities. He is currently a Senior Researcher with the National Institute of Advanced Industrial Science and Technology, Tokyo, Japan. His research interests include optical switches and integrated silicon optical circuits. He was

the recipient of an APL Photonics Future Luminary Award in 2020.

**Keijiro Suzuki** received the B.E. and M.E. degrees from the Department of Electrical and Electronic Engineering, Shizuoka University, Hamamatsu, Japan, in 2004 and 2006, respectively, and the Ph.D. degree from Yokohama National University (YNU), Yokohama, Japan, in 2011. After spending two years with Sumitomo Osaka Cement Co., Ltd., he entered the Department of Electrical and Computer Engineering, Yokohama National University, in 2008 and was awarded a Research Fellowship for Young Scientists from JSPS. After spending one year with YNU as a Postdoctoral Fellow, he joined the National Institute of Advanced Industrial Science and Technology, Tsukuba, Japan, in 2012. He is a Member of the OSA, IEICE, and JSAP. His research interests include photonic integrated circuits, nanophotonics, and nonlinear optics.